Symmetry-broken Chern insulators and Rashba-like Landau-level crossings in magic-angle bilayer graphene

Ipsita Das[1,4], Xiaobo Lu[1,4 ✉], Jonah Herzog-Arbeitman[2], Zhi-Da Song[2], Kenji Watanabe[3], Takashi Taniguchi[3], B. Andrei Bernevig[2] and Dmitri K. Efetov[1 ✉]

Flat bands in magic-angle twisted bilayer graphene (MATBG) have recently emerged as a rich platform to explore strong correlations[1], superconductivity[2–5] and magnetism[3,6,7]. However, the phases of MATBG in a magnetic field and what they reveal about the zero-field phase diagram remain relatively uncharted. Here we report a rich sequence of wedge-like regions of quantized Hall conductance with Chern numbers $C = \pm 1, \pm 2, \pm 3$ and ± 4, which nucleate from integer fillings of the moiré unit cell $\nu = \pm 3, \pm 2, \pm 1$ and 0, respectively. We interpret these phases as spin- and valley-polarized many-body Chern insulators. The exact sequence and correspondence of the Chern numbers and filling factors suggest that these states are directly driven by electronic interactions, which specifically break the time-reversal symmetry in the system. We further study the yet unexplored higher-energy dispersive bands with a Rashba-like dispersion. The analysis of Landau-level crossings enables a parameter-free comparison to a newly derived 'magic series' of level crossings in a magnetic field and provides constraints on the parameters of the Bistritzer–MacDonald MATBG Hamiltonian. Overall, our data provide direct insights into the complex nature of symmetry breaking in MATBG and allow for the quantitative tests of the proposed microscopic scenarios for its electronic phases.

Electron interactions can break the underlying symmetries of condensed matter systems and drive the formation of various quantum phases. In twisted bilayer graphene (tBLG) rotated by the magic angle of $\theta_m \approx 1.1°$, ultraflat moiré bands[8] host strongly interacting electrons that give rise to phases including correlated insulators[1,9,10], superconductors[2–5] and orbital magnets[3,6,7]. The variety of phases observed in magic-angle twisted bilayer graphene (MATBG) suggests the presence of interesting low-energy states in the many-body spectrum, some of which can be stabilized by external tuning parameters such as pressure, strain and fields. However, the exact nature of the interaction-driven symmetry-broken ground states is still not well understood. Recently, it was proposed that the two-spin valley-degenerate flat bands can be understood as a series of eightfold (quasi-) degenerate topologically non-trivial bands with opposite Chern numbers $C = 1$ and $C = -1$ (refs. [11,12]), with recent experimental evidence mounting in favour of this picture[5,13–15]. Moreover, the nature of the high-energy dispersive bands and the possible phases that can appear at higher filling factors have not been explored.

To reveal the topologically non-trivial properties of the low-energy states of MATBG, it is necessary to lift their degeneracy by creating an energy gap between them. The single-particle band structure of MATBG obeys the inversion and time reversal of the C_2 and T symmetries, which protects the Dirac points. Breaking this symmetry can create a gap and give rise to Chern insulators with quantized Hall conductance. This has been achieved in the past by breaking the C_2 lattice symmetry at the single-particle level by structural alignment with hexagonal boron nitride (hBN) substrates[6,7]. Recent studies have also observed Chern insulators in devices without alignment to the hBN and hence without explicit single-particle symmetry breaking[3,5]. For these samples, strong electronic interactions could directly break one or both the C_2 and T symmetries and valley polarize the system, creating isolated (quasi-) flat bands in the K and K' valleys and giving rise to a sequence of quantum Hall ferromagnets.

Here we report studies of tBLG devices close to the first magic angle $\theta = 1.03–1.15°$, which were not specifically aligned to the hBN substrates. Figure 1a shows the schematic of the typical devices, which consist of a quadruple van der Waals heterostructure of graphite/hBN/MATBG/hBN. We perform four-terminal longitudinal resistance (R_{xx}) and Hall resistance (R_{xy}) measurements, where the carrier concentration n in the MATBG is continuously controlled by voltage V_g at the graphite gate. We normalize n by $n_S = 4n_0$, where n_S is the density of the fully filled fourfold spin- and valley-degenerate moiré bands and n_0 is the density per flavour; further, the filling factor of the carriers per moiré unit cell is defined as $\nu = n/n_0$. Applying a perpendicular magnetic field $B_\perp$ at $T = 1.5$ K (Fig. 1b,c) reveals a set of broad wedge-shaped regions in the n–B phase space, where $R_{xx} \approx 0\,\Omega$ and $R_{xy} \approx h/Ce^2$ (where e is the electron charge and h is Planck's constant). These quantized regions follow a linear slope of $dn/dB = Ce/h$, which can be traced to different integer fillings ν at $B = 0$. These singular states show a clear correspondence between the Chern number and filling factor (C, ν). We find a robust sequence for the $(\pm 4, 0)$, $(\pm 3, \pm 1)$, $(\pm 2, \pm 2)$ and $(\pm 1, \pm 3)$ states in different devices, as shown in Fig. 1e, showing the schematic of their cumulative phase diagrams.

At lower T, we also observe a clear set of Landau-level (LL) fans, which follow the typically reported fourfold degeneracy at the charge neutrality point (Supplementary Fig. 3). The energy gaps associated with these states are up to an order of magnitude smaller than the gaps of the (C, ν) states, which have values of $\Delta \approx 1$ meV (Supplementary Information). The (C, ν) states are more visibly pronounced, and some already quantize below $B_\perp < 0.3$ T and $T < 10$ K (Supplementary Fig. 6). This is in contrast to LL quantization,

[1]ICFO—Institut de Ciències Fotòniques, The Barcelona Institute of Science and Technology, Castelldefels, Barcelona, Spain. [2]Department of Physics, Princeton University, Princeton, NJ, USA. [3]National Institute for Materials Science, Tsukuba, Japan. [4]These authors contributed equally: Ipsita Das, Xiaobo Lu. ✉e-mail: xiaobo.lu@icfo.eu; dmitri.efetov@icfo.eu
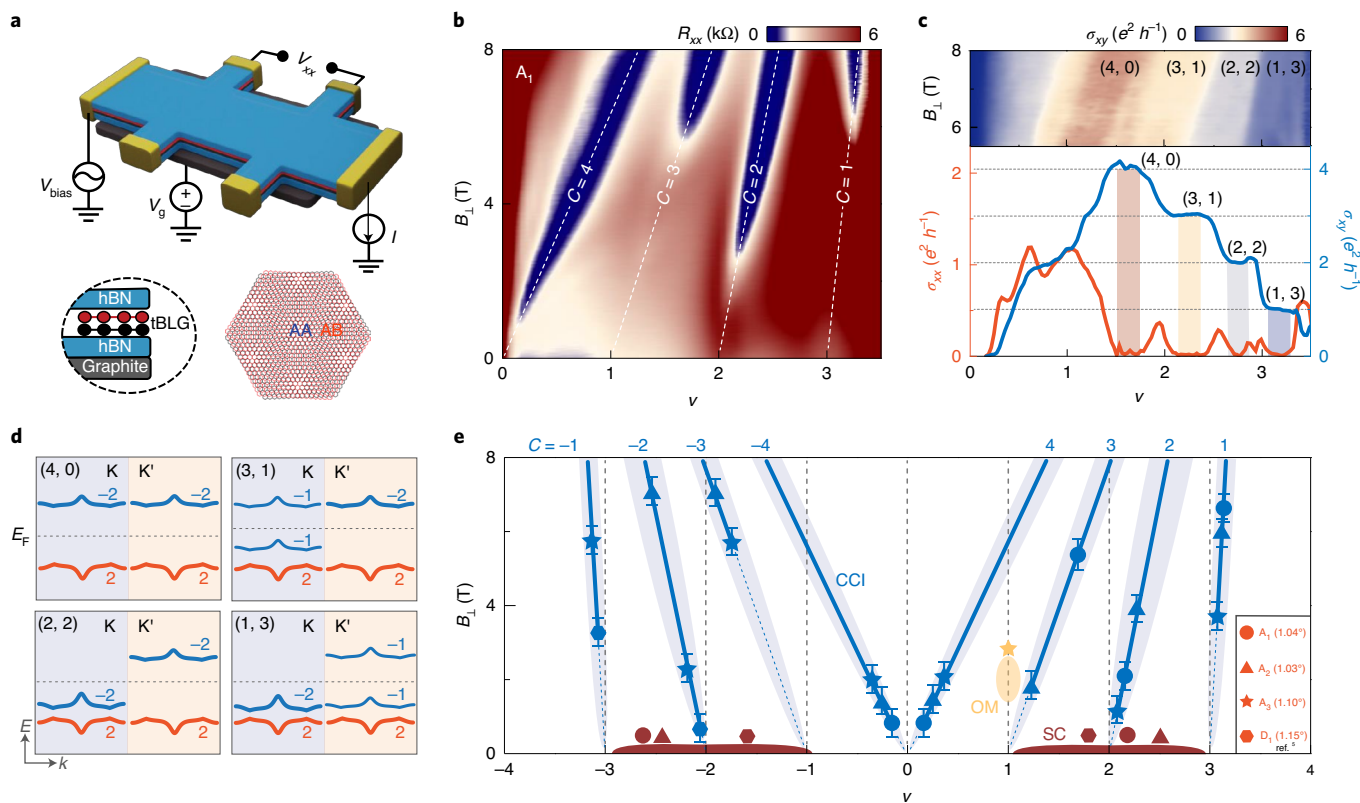
Fig. 1 | Emergent CCIs in MATBG. a, Schematic and cross-section of the hBN-encapsulated graphite-gated MATBG device. A moiré pattern with periodically alternating regions of AA and AB stacking is formed between the graphene layers. Four terminal transport measurements are achieved by application of an alternating bias voltage V_{bias} across the device and reading out of the voltage drop V_{xx} and the resulting current I. **b**, Colour plot of R_{xx} versus ν and $B_\perp$, measured at $T = 1.5$ K. The white lines indicate the trajectories of four different topologically non-trivial Chern gaps with (C, ν) indices of (4, 0), (3, 1), (2, 2) and (1, 3). **c**, Corresponding Hall conductance σ_{xy} versus ν and $B_\perp$ (top) and line cuts showing quantized σ_{xy} and vanishing longitudinal conductance of the Chern insulators at $B_\perp = 8$ T (bottom). **d**, Schematic of the proposed band arrangement sequence for the symmetry-broken topological bands and CCIs at different fillings ($\nu = 0, 1, 2$ and 3), as a function of energy E and momentum k, where E_F marks the position of the Fermi energy. We note that a valley-coherent configuration for the (2, 2) state is also allowed (Supplementary Fig. 10). **e**, Schematic of the cumulative phase diagram for several devices, summarizing the observed CCI, superconductor (SC) and orbital magnet (OM) in the ν–$B_\perp$ plane. The position of the device icons for each CCI corresponds to the critical $B_\perp$-field values (uncertainties indicated by the error bars are defined by the full-width at half-minimum values of $dR_{xx}/dB_\perp$ versus $B_\perp$ for fixed C) at which these states form. Similarly, the optimal doping positions for SC are marked by the corresponding device icons.

where MATBG typically occurs above $B_\perp > 3$ T and below $T < 1$ K. This allows us to disentangle these gaps by elevating T and to observe their robust and unperturbed sequence. However, these states do not form in a zero $B_\perp$ field; even though they require a $B_\perp$ field to nucleate, the $(\pm 4, 0)$, (3, 1) and $(-2, -2)$ states already form at a negligibly small $B_\perp > 0.1$ T. The very small values of the field for which these states appear, especially the $(-2, -2)$ state[12], suggests that they are very competitive to the true ground state in the zero field. In contrast, the $(-3, -1)$ and $(\pm 1, \pm 3)$ states require higher fields of $B_\perp > 2$ T. Figure 1e summarizes the corresponding critical $B_\perp$ fields for all the states and devices.

We interpret these states as correlated Chern insulators (CCIs) that are driven by interactions and stabilized by a small $B_\perp$ field. These states are possible because the underlying flat bands of MATBG can be thought of as Chern bands with eightfold valley, spin and sub-lattice degeneracy, which carry opposite Chern numbers $C = 1$ and $C = -1$ (refs. [11–15]). Lifting the degeneracy of these bands by gaping out their Dirac points and polarizing them can create topologically non-trivial gaps. This is analogous to the interaction-driven formation of quantum Hall ferromagnets from degenerate LLs in large B fields, although the microscopic origins are distinct[16–18]. In MATBG, the flat moiré bands allow interactions to dominate and open CCI states in the zero B-field limit.

Chern bands are known to be favourable in MATBG: due to the topology of the active bands, any bandgap opening creates individual non-zero Chern bands (whose total Chern number adds to zero without interactions). However, valley or spin ferromagnetism then polarizes the Chern bands to create ground states with non-zero Chern number. Moreover, the robust sequence for the $(\pm 4, 0)$, $(\pm 3, \pm 1)$, $(\pm 2, \pm 2)$ and $(\pm 1, \pm 3)$ states strongly constrain the underlying band topology and driving mechanisms. To explain the data, interactions that break T rather than break the C_2 symmetry are required[14]. Overall, this picture can well explain the observed pecking order of the Chern numbers between the neighbouring states. This indicates that starting from $\nu = 0$, the total Chern number of $C = 4$ is decreased by 1 when ν is increased to the next integer value on the electron side. Equivalently, on the hole side, starting from $C = -4$ at $\nu = 0$, C increases by 1 when ν is decreased to the next integer value. This can be understood as the repeated filling of the correlation-induced valley-/spin-polarized sub-bands with Chern numbers $C = -1$ for electrons and $C = 1$ for holes[13–15] (Fig. 1d).

The exact sequence of Chern numbers at different fillings gives an insight into the dominant symmetry-breaking mechanisms. Unlike in previous studies, where C_2 symmetry was deliberately broken by the alignment of MATBG with hBN substrates, we avoid this by keeping the angle between the crystallographic orientations of
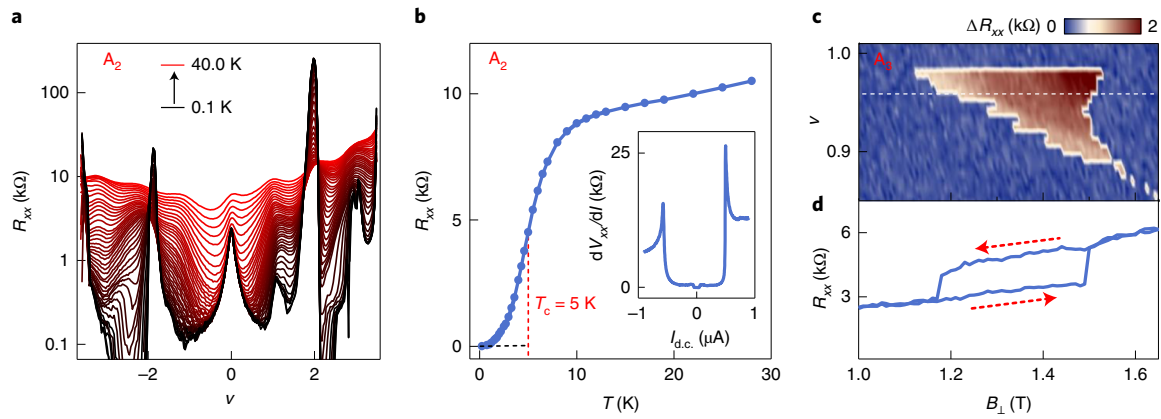
Fig. 2 | Correlated insulators, superconductors and orbital magnets in MATBG. a, R_{xx} versus ν of device A_2 at different temperatures, which shows the well-developed Chern insulator at $\nu=\pm2$ and the superconducting regions. **b**, Temperature dependence of R_{xx} at optimal doping ($\nu=2.5$) showing a critical temperature $T_c=5$ K, which is defined as the temperature of the 50% normal-state resistance. The inset shows differential resistance measurements dV_{xx}/dI versus bias current I, showing a sharp superconducting critical current transition. **c**, Hysteresis loop reveals an orbital magnet state in device A_3 at filling of $\nu=0.96$ and $T=100$ mK (bottom), which exists only in a narrow window of filling and $B_\perp$ field, which is seen by the non-zero resistance change between the up and down sweeps (ΔR_{xx}) (top).

MATBG and hBN as $\theta>10°$. Generally, broken C_2 symmetry (and keeping T unbroken) leads to a sign reversal of the Chern numbers in the K and K' valleys; in contrast, broken T symmetry (and keeping C_2 unbroken) is expected to preserve their Chern numbers. This can have a clear impact on the resulting many-body states and the predicted Chern numbers for each ν. As shown in Supplementary Fig. 10, while breaking either symmetry at charge neutrality as a parent state of the other fillings predicts the $(\pm2, \pm2)$ and $(\pm1, \pm3)$ states, C_2 breaking predicts the existence of the $(\pm1, \pm1)$ and $(0, 0)$ states, instead of the $(\pm3, \pm1)$ and $(\pm4, 0)$ states predicted from the breaking of T symmetry and observed in the experiment[13–15]. We, therefore, suggest that the interactions in the $B_\perp$ field in MATBG specifically break the T symmetry at $\nu=0$ and break both T and C_2 symmetries at $\nu=\pm1$ and ±3.

A central question is why the Chern insulators require a non-zero $B_\perp$ field to nucleate. Since the $(\pm4, 0)$, $(3, 1)$ and $(-2, -2)$ states already occur in the weak-field limit as low as $B_\perp\approx0.1$ T corresponding to a negligibly small magnetic flux per moiré unit cell of only $\Phi<0.01\Phi_0$ (where Φ_0 is the flux quantum), we find it unlikely that the onset of the Hofstadter sub-bands is responsible. Because T breaking is crucial to the observed sequence of Chern states, we would expect the application of weak $B_\perp$ to stabilize this phase because the applied magnetic field breaks the T symmetry (but not C_2). At $B_\perp=0$, the many-body states of different Chern numbers, including topologically trivial $C=0$ states, closely compete with one another in energy and are obscured by disorder, but the application of $B_\perp$ energetically favours the states with higher C values[19–21]. Hence, our proposed scenario of a T-broken CCI is supported by the appearance of such states at non-zero $B_\perp$. A further many-body study suggests that at $\nu=\pm1$, the $C=\pm1$ and ±3 states are degenerate in the Coulomb Hamiltonian projected to the active bands[22]. When a magnetic field is added, the $C=\pm3$ bands become energetically favourable[22].

The symmetry and topology of the underlying ground state has dramatic implications for the understanding of the possible mechanisms responsible for all the other emergent phases, which can also be observed in the reported devices (Fig. 1e and Fig. 2a–c). Their phase space lies close to the Chern insulators, where most samples are robust superconductors and topologically trivial insulators around $\nu=\pm2$. In particular, device A_2 shows a critical superconducting temperature for MATBG devices of $T_c\approx5$ K (Fig. 2b), as well as strong resistance peaks at half filling that interrupt the

superconducting domes (Fig. 2a). However, in the previously reported device D_1 (ref. [5]), we did not observe a $C=0$ insulator at $\nu=-2$; instead, we found a broad superconducting dome region and a $(C=-2)$-correlated insulator formed above $B_\perp>0.2$ T. In addition, in device A_3, at $\nu=1$, we observe an orbital magnet at $B_\perp\approx2$ T very close to forming a correlated insulator (Fig. 2c), likely created through a similar microscopic mechanism. Overall, these findings may suggest a close competition between topologically trivial and non-trivial insulators at $B_\perp=0$, which directly impacts the superconductor and orbital magnet phases.

We further tune the carrier density beyond the full filling of the flat bands at $|\nu|>4$ and populate the largely unstudied higher-energy dispersive bands of MATBG. Figure 3a shows the calculated energy dispersion of MATBG using the Bistritzer–MacDonald model[8] including corrugations (Supplementary Discussions 10 and 11). The two lowest-lying fourfold degenerate higher-energy bands can be modelled with a Rashba-like Hamiltonian, that is, a two-band model to order $O(k^2)$ that transitions from a Dirac point into quadratic free-electron bands (Fig. 3b). The model can be justified by a perturbative calculation, and the trigonal distortion terms are also computed (Supplementary Discussion 12). The Rashba-like Hamiltonian does not originate from the spin–orbit coupling, which is negligible in these samples, but from the crystalline terms. In this regime, we perform $B_\perp$-field-dependent R_{xx} versus ν measurements, which reveal a rich fourfold degenerate LL spectrum with a multitude of well-pronounced LL crossings[23–25], Hofstadter sub-bands and a new set of LLs at $|\nu|=8$ (Fig. 3c). These features are well developed in all devices and show relatively symmetric electron–hole features in the valence and conduction bands.

We exactly solve the Rashba Hamiltonian in the $B_\perp$ field and obtain the LLs (Supplementary Discussion 10), which are in excellent quantitative agreement with the experimental findings. The calculation reveals a series of LLs, each carrying the Chern number $C=4$, which interpolate between the Dirac node and quadratic free-electron regimes. Critically, all the LLs undergo a series of crossings, or gap closings, as calculated (Supplementary Discussion 10) and experimentally seen in the R_{xx} versus ν and $B_\perp$ measurements close to the bandgaps (Fig. 3c); for clarity, Fig. 3f shows the conversion of the same data into R_{xx} versus C and $1/B_\perp$. The LL crossing between the nth and $(n+1)$th LLs happen in the well-defined field of $B_\perp=B^*$ (Fig. 3d), and it can be understood as an interruption of the LL gap with $C=n$ in the LL fan diagram. However, the gap
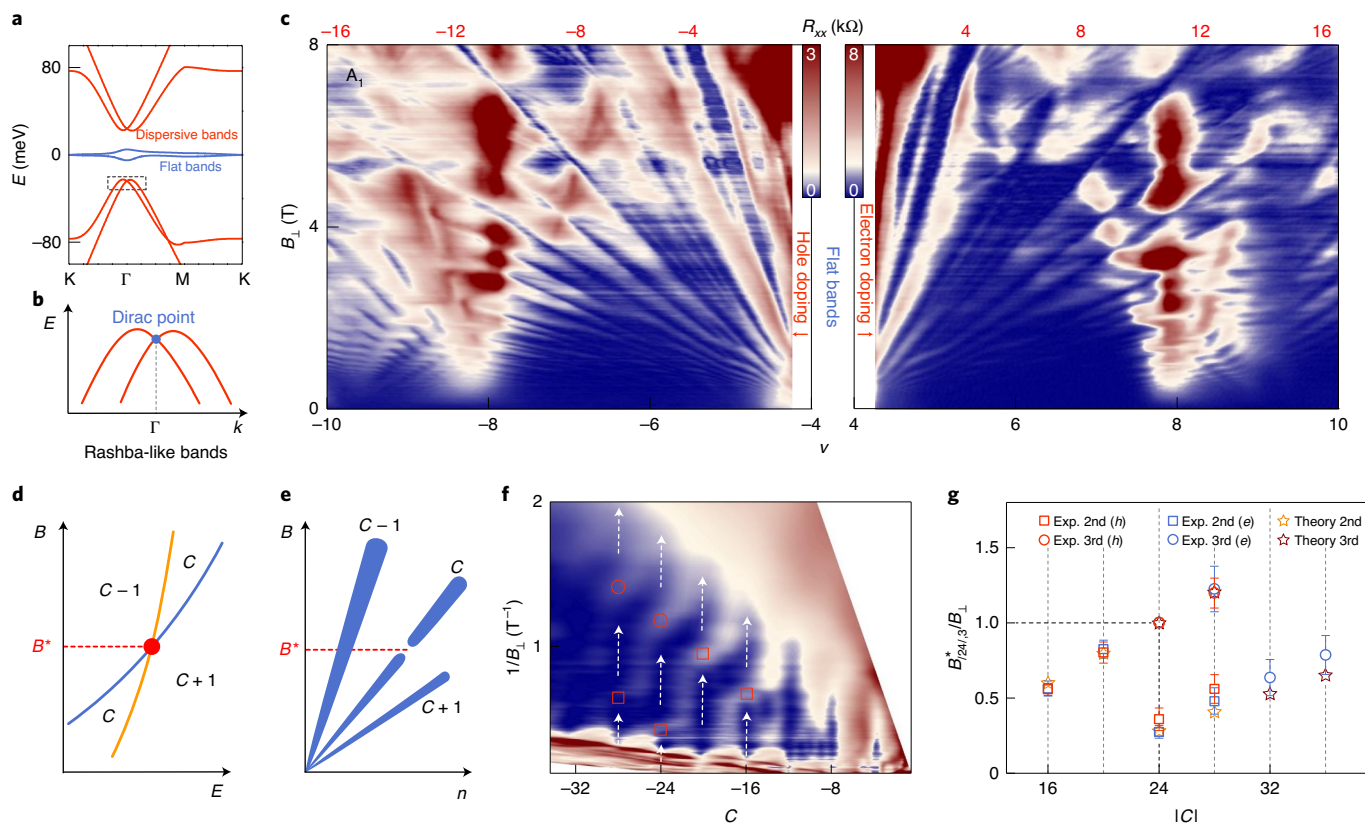
Fig. 3 | Rashba-like bands and LL crossings in higher-energy dispersive bands. a, Band structure (single valley and single spin) of MATBG. **b**, Zoomed-in view of the higher-energy dispersive bands, which can be approximated by a Rashba-like energy dispersion. **c**, Colour plot of R_{xx} versus ν and $B_\perp$ measured at $T = 30$ mK, where the Chern numbers of the most dominant LL gaps are marked. **d**, Illustration of the LL gap closings by two intersecting LLs at B^*. **e**, Corresponding LL fan diagram in the n–$B_\perp$ plane shows interrupted LL gaps. **f**, Colour plot of R_{xx} versus C and $1/B_\perp$ (with data from the hole side of **c**), showing interrupting trajectories of the different LL gaps; the corresponding gap closings are marked. **g**, Comparison of the experimentally observed LL gap closings (Exp. 2nd, Exp. 3rd) and the theoretically predicted (Theory 2nd, Theory 3rd), normalized to $B^*_{|24|,3}$, the field of the third-generation gap closing of the $C = \pm 24$ LL gaps (for electrons and holes, respectively). The error bars are defined by the full-width at half-maximum values of R_{xx} versus $1/B_\perp$ peaks where the LL crossings occur.

reappears at a higher field (Fig. 3e). Each LL gap is interrupted several times, where we count the different generations of crossings for each LL from high to low $B_\perp$. We extract the B^* values for all the LL crossings (from Fig. 3c,f); normalize these to $B^*_{|24|,3}$, which is the field at the third crossing of the LL at $C = \pm 24$ (for electrons and holes, respectively); and fit them with our calculations shown in Fig. 3g. This allows us to extract an estimate of the Rashba coupling parameter ξ (Supplementary Discussions 10–12). Moreover, we find that the ratios between all the B^* values are independent of all the parameters of the low-energy Hamiltonian and therefore present a stringent, parameter-free test of the physics—we call this the 'magic series'. The two corrugation parameters w_0 and w_1 of the Bistritzer–MacDonald Hamiltonian are constrained by the measured Rashba coupling $\xi = 0.186/\Omega$ ($h = 1$ and $\Omega = \sqrt{3}/2(13.5\,\text{nm})^2$ is the area of the moiré unit cell), presenting a direct estimation of the physical parameters of MATBG (Supplementary Discussions 10–12). Neglecting the particle–hole symmetry breaking, we find that the ranges $0.7 \leq w_0/(v_F k_D/\sqrt{3}) \leq 0.80$ and $0.95 \leq w_1/(v_F k_D/\sqrt{3})$ are in good agreement with the measurements of the Rashba coupling, where v_F is the Fermi velocity and k_D is the moiré wavevector[19,20,26].

In summary, our data provide a new and detailed view of the high-$B_\perp$-field phase diagram of MATBG and demonstrate its underlying topologically non-trivial properties. The topological nature of the flat bands in MATBG observed in this study has implications for the potential understanding of the superconducting phase, which needs to be understood on the basis of the ground states found here;

further, this could be considered as topological superconductivity[27]. To further comprehend the microscopic mechanisms driving the CCI and interactions between the various quantum states (CCI, superconductor and orbital magnet), one possible direction is to control the correlated states by inducing dielectric screening or spin–orbit coupling in higher-quality devices in further experiments[5,28,29].

Online content

Any methods, additional references, Nature Research reporting summaries, source data, extended data, supplementary information, acknowledgements, peer review information; details of author contributions and competing interests; and statements of data and code availability are available at https://doi.org/10.1038/s41567-021-01186-3.

References

1. Cao, Y. et al. Correlated insulator behaviour at half-filling in magic-angle graphene superlattices. *Nature* **556**, 80–84 (2018).
2. Cao, Y. et al. Unconventional superconductivity in magic-angle graphene superlattices. *Nature* **556**, 43–50 (2018).
3. Lu, X. et al. Superconductors, orbital magnets and correlated states in magic-angle bilayer graphene. *Nature* **574**, 653–657 (2019).

4. Yankowitz, M. et al. Tuning superconductivity in twisted bilayer graphene. *Science* **363**, 1059–1064 (2019).
5. Stepanov, P. et al. Untying the insulating and superconducting orders in magic-angle graphene. *Nature* **583**, 375–378 (2020).
6. Sharpe, A. L. et al. Emergent ferromagnetism near three-quarters filling in twisted bilayer graphene. *Science* **365**, 605–608 (2019).
7. Serlin, M. et al. Intrinsic quantized anomalous Hall effect in a moiré heterostructure. *Science* **367**, 900–903 (2020).
8. Bistritzer, R. et al. Moiré bands in twisted double-layer graphene. *Proc. Natl Acad. Sci. USA* **108**, 12233–12237 (2011).
9. Wong, D. et al. Cascade of electronic transitions in magic-angle twisted bilayer graphene. *Nature* **582**, 198–202 (2020).
10. Zondiner, U. et al. Cascade of phase transitions and Dirac revivals in magic-angle graphene. *Nature* **582**, 203–208 (2020).
11. Song, Z. et al. All magic angles in twisted bilayer graphene are topological. *Phys. Rev. Lett.* **123**, 036401 (2019).
12. Liu, J. et al. Pseudo Landau level representation of twisted bilayer graphene: band topology and implications on the correlated insulating phase. *Phys. Rev. B* **99**, 155415 (2019).
13. Wu, S. et al. Chern insulators and topological flat-bands in magic-angle twisted bilayer graphene. Preprint at https://arxiv.org/abs/2007.03735 (2020).
14. Nuckolls, K. P. et al. Strongly correlated Chern insulators in magic-angle twisted bilayer graphene. *Nature* **588**, 610–615 (2020).
15. Saito, Y. et. al. Hofstadter subband ferromagnetism and symmetry broken Chern insulators in twisted bilayer graphene. *Nat. Phys.* https://doi.org/10.1038/s41567-020-01129-4 (2021).
16. Nomura, K. et al. Quantum Hall ferromagnetism in graphene. *Phys. Rev. Lett.* **96**, 256602 (2006).
17. Young, A. F. et al. Spin and valley quantum Hall ferromagnetism in graphene. *Nat. Phys.* **8**, 550–556 (2012).
18. Song, Y. J. et al. High-resolution tunnelling spectroscopy of a graphene quartet. *Nature* **467**, 185–189 (2010).
19. Tschirhart, C. L. et al. Imaging orbital ferromagnetism in a moiré Chern insulator. Preprint at https://arxiv.org/abs/2006.08053 (2020).
20. Lian, B. et al. TBG IV: exact insulator ground states and phase diagram of twisted bilayer graphene. Preprint at https://arxiv.org/abs/2009.13530 (2020)
21. Tarnopolsky, G. et al. Origin of magic angles in twisted bilayer graphene. *Phys. Rev. Lett.* **122**, 106405 (2019).
22. Stepanov, P. et al. Competing zero-field Chern insulators in superconducting twisted bi-layer graphene. Preprint at https://arxiv.org/abs/2012.15126 (2020)
23. Taychatanapat, T. et al. Quantum Hall effect and Landau-level crossing of Dirac fermions in trilayer graphene. *Nat. Phys.* **7**, 621–625 (2011).
24. Datta, B. et al. Strong electronic interaction and multiple quantum Hall ferromagnetic phases in trilayer graphene. *Nat. Commun.* **8**, 14518 (2017).
25. Uri, A. et al. Mapping the twist-angle disorder and Landau levels in magic-angle graphene. *Nature* **581**, 47–52 (2020).
26. Po, H. et al. Faithful tight-binding models and fragile topology of magic-angle bilayer graphene. *Phys. Rev. B* **99**, 195455 (2019).
27. Xu, C. et al. Topological Superconductivity in twisted multilayer graphene. *Phys. Rev. Lett.* **121**, 087001 (2018).
28. Liu, X. et al. Tuning electron correlation in magic-angle twisted bilayer graphene using Coulomb screening. Preprint at https://arxiv.org/abs/2003.11072 (2020).
29. Arora, H. et al. Superconductivity in metallic twisted bilayer graphene stabilized by WSe_2. *Nature* **583**, 379–384 (2020).

Methods

Device fabrication. The MATBG samples were fabricated using a 'cut-and-stack' method. The graphene was cut into two pieces using an AFM tip to prevent any unintentional strain during the tearing process. Then, a stamp of poly(bisphenol A carbonate)/polydimethylsiloxane mounted on a glass slide was used to pick up an hBN flake (typically 10–15 nm thick) at 100–110 °C. The hBN flake was then used to carefully pick up the first half of the pre-cut graphene piece from the Si^{++}/SiO_2 (285 nm) substrate. The second layer of graphene was rotated by a target angle of $\theta = 1.1–1.2°$ and simultaneously picked up by the hBN/graphene stack from the last step at 100 °C. Subsequently, another hBN layer was picked up to completely cover the tBLG. The final layer of the heterostructure consists of a few layers of graphite, which acts as a local back gate. In the end, poly(bisphenol A carbonate) was melted at 180 °C and the full stack was dropped on an O_2-plasma-cleaned Si^{++}/SiO_2 chip. The electrical connections to the tBLG were made by CHF_3/O_2 plasma etching and deposition of Cr/Au (6 nm/50 nm) as the metallic edge contacts.

Measurements. All our transport measurements were carried out in a dilution refrigerator (Bluefors SD250) with a base temperature of 20 mK. We have used a standard low-frequency lock-in technique (Stanford Research SR860 amplifiers) with an excitation frequency $f = 13.111$ Hz. To achieve a lower electron temperature in our measurements, we used a very low excitation current (10 nA) owing to the risk of overheating electrons and fragility of the superconductivity phases. Keithley 2400 voltage sourcemeters were used to control the back-gate voltage. The differential resistance dV_{xx}/dI (where V_{xx} is the voltage drop and I is the resulting current) was measured with an a.c. excitation current (1 nA) applied through an a.c. signal generated by the lock-in amplifier in combination with a 10 MΩ resistor. A d.c. bias current was applied through a 1/100 divider and a 1 MΩ resistor before combining with the a.c. excitation. The as-induced differential voltage was further measured at the same frequency (19.111 Hz) with the standard lock-in technique. We also performed the electronic filtering of the measurement setup using a network of commercially available low-pass RC and LC filters.

Twist angle extraction. The phase diagrams shown in Supplementary Figs. 3–5 are used to estimate the twist angle θ in the measured devices. We use the relation $n_S = 8\theta^2/\sqrt{3}a^2$, where $a = 0.246$ nm is the lattice constant of graphene and n_S is the charge carrier density corresponding to a fully filled superlattice unit cell. Quantum oscillations propagating outside the fully filled flat band were used to define n_S. The carrier density was calibrated with the trajectory of LLs and low-field Hall effect. The twist angles are as follows: A_1, ~1.04°; A_2, ~1.03°; A_3, ~1.10°.

Data availability

All data that support the plots within this paper and other findings of this study are available from the corresponding authors upon reasonable request.

Author contributions

D.K.E., X.L. and I.D. conceived and designed the experiments. I.D. and X.L. performed the device fabrication and transport measurements. J.H.-A., Z.-D.S. and B.A.B. performed the theoretical modelling of the data. K.W. and T.T. provided the hBN crystals. I.D., X.L., J.H.-A., Z.-D.S., B.A.B. and D.K.E. analysed the data and wrote the paper.

Competing interests

The authors declare no competing interests.

Additional information

Supplementary information The online version contains supplementary material available at https://doi.org/10.1038/s41567-021-01186-3.

Correspondence and requests for materials should be addressed to X.L. or D.K.E.

Peer review information *Nature Physics* thanks Shubhayu Chatterjee, Feng Wang and Ke Wang for their contribution to the peer review of this work.

Reprints and permissions information is available at www.nature.com/reprints.